CFD Analyses of Different Parameters Influencing the Hemodynamic Outcomes of Complex Aortic Endovascular Repair

Sabrina Ben-Ahmed, Jean-Noël Albertini, Jean-Pierre Favre, C Alberto Figueroa, Eugenio Rosset, Francesca Condemi, Stéphane Avril

Chapter **1**

CFD Analyses of Different Parameters Influencing the Hemodynamics Outcomes of Complex Aortic Endovascular Repair

Sabrina BEN-AHMED

Service de Chirurgie Vasculaire et Médecine Vasculaire, CHU Limoges, F-87000 Limoges, France.

Jean-Noël ALBERTINI and Jean-Pierre FAVRE

Service de Chirurgie Cardiovasculaire, CHU Saint-Étienne, F-42000 Saint-Étienne, France.

C. Alberto FIGUEROA

Department of Biomedical Engineering, University of Michigan, Ann Arbor, MI, USA.

Eugenio ROSSET

Service de Chirurgie Vasculaire, CHU Clermont-Ferrand, INSERM, Université Clermont Auvergne, F-63003, France.

Francesca CONDEMI and Stéphane AVRIL

Mines Saint-Étienne, Univ Lyon, Univ Jean Monnet, INSERM, U1059 Sainbiose, Centre CIS, F-42023 Saint-Étienne, France.

1.1. Introduction

Over the past decades, technologies in endovascular aortic aneurysm repair (EVAR) have evolved rapidly. Complex abdominal aneurysms with unfavorable neck (i.e. very short length of normal aorta between the lowest renal artery and the beginning of aneurysmal dilatation) or involving renal or digestive arteries are unsuitable for conventional EVAR. They carry high risk for open surgery, with a high rate of renal complications (West *et al*. (2006)). Innovative minimally invasive approaches such as fenestrated (fEVAR), chimney (chEVAR) or periscope EVAR (pEVAR) were developed to treat complex aortic aneurysms and to preserve target vessel perfusion. The advantages of these endovascular techniques over conventional open repair are the reduction of mortality and morbidity (such as blood loss and complications related to aortic and visceral arterial clamping that could lead to organ ischemia)(O'Donnell *et al*. (2019), Verhoeven *et al*. (2010, 2015), Oderich *et al*. (2014), O'neill *et al*. (2006), Nordon *et al*. (2009)). The fEVAR devices include custom-made fenestrated stentgrafts which usually take several weeks to be manufactured and consequently, they are not available in emergency situations. Parallel stentgraft techniques such as chEVAR and pEVAR, are built using off-the-shelf devices with antegrade parallel renal stentgrafts (chEVAR) or retrograde parallel renal stentgrafts (pEVAR) associated to a main aortic endograft. Their main advantage is immediate availability. The different repair methodologies (fEVAR, chEVAR and pEVAR) may impact hemodynamics in target vessels such as the renal arteries, a major concern in EVAR. Renal events often complicate complex EVAR such as target vessel loss (3-4%), renal stenosis (7%) or postoperative renal dysfunction (20 to 29%) (Mohabbat *et al*. (2009), Ou *et al*. (2015), Tran *et al*. (2016), Martin-Gonzalez *et al*. (2015)). Renal dysfunction may arise from perioperative arterial lesions caused by the device (Mohabbat *et al*. (2009)) or from strong hemodynamic alterations following the procedure. Intrastent stenosis and thrombosis after stent implantation remain major clinical issues. Wall motion and flow disturbances distal to the stentgraft are associated with increased intimal hyperplasia, particularly at the junction between the stent and the artery. The mechanisms are not fully understood, but direct endothelial damage, reduced compliance, alteration of the distribution of the wall shear stress (WSS) within the stentgraft (LaDisa Jr *et al*. (2005)) may be involved. Restenosis from intimal hyperplasia is often observed at the distal ends of the stent (Sutton *et al*. (1988)). The stent rigidity relative to the native arterial compliance results in stiffness mismatch (LaDisa Jr *et al*. (2005)), which may also stimulate intimal hyperplasia. Moreover, since the aorta is fixed at the retroperitoneum, the proximal segment of the renal arteries undergoes limited motion compared to its distal counterpart. Moreover, respiration may cause kidney rigid-body motion leading to upward and downward deflections of the renal arteries, with a larger displacements distally than close to renal ostia (Draney *et al*. (2005)). This mobility again may contribute to intimal hyperplasia. Nevertheless it should be noted that the stented length is usually greater in parallel stentgraft techniques than in

	Proximal Resistance $g/(mm^4.s)$	Compliance $mm^4.s^2/g$	Distal resistance $g/(mm^4.s)$
Right Renal Artery	0.51	1.96	2.08
Left Renal Artery	0.51	1.96	2.08
Right Iliac Artery	0.11	4.96	0.81
Left Iliac Artery	0.11	4.96	0.81

Table 1.1. *Boundary conditions of the renal and iliac outlets.*

fEVAR (Ullery *et al*. (2016)). Analyzing renal artery hemodynamics following fEVAR, chEVAR and pEVAR may help to understand the occurrence of renal complications such as intrastent or arterial stenosis from intimal hyperplasia or thrombosis in the renal arteries. Computational fluid dynamics (CFD) is a tool that enables detailed investigation and systematic comparison of hemodynamic descriptors in complex EVAR. Our aim was to analyze the hemodynamic impacts of fenestrated, chimneys and periscopes endovascular repair of complex abdominal aortic aneurysms on renal arteries. The study reported in the present paper focused on the patterns of flow, pressure and WSS caused by complex EVAR and by the possible stenosis related to intimal hyperplasia. The influence on platelet transport and activation was also considered. Understanding the hemodynamic impact of different EVAR procedures can potentially help clinicians to prevent renal complications and to make optimal choices between the types of EVAR procedures (fEVAR vs chEVAR or fEVAR vs pEVAR).

1.2. Methods

A series of 9 idealized computed aided design (CAD) models of complex EVAR was created in Autodesk Inventor 2016. These models were divided in 3 groups: fEVAR, chEVAR and pEVAR. In each group, 3 models were created with different degrees of renal arterial stenosis: no stenosis (baseline model), a non clinically significant stenosis : 40%-diameter reduction and a clinically significant one : 70%-diameter reduction. The 40% stenosis is a non hemodynamically stenosis, whereas the 70% stenosis represents a hemodynamically stenosis that leads to hemodynamically significant reductions in renal blood flow and pressures. The stenoses were created 2 cm after the renal ostium at both right and left renal arteries. They represent the intimal hyperplasia usually developed at the junction between the renal artery and the distal part of the renal stentgraft (Sutton *et al*. (1988), Draney *et al*. (2005)). All models were built with equal aortic inlet diameter (24 mm), iliac artery diameter (12 mm), renal artery diameter (6 mm) and length (62 mm). The total length of the fEVAR and pEVAR models was equal (286 mm). The chEVAR model was larger (339 mm) to minimize the disturbances triggered by the chimney inlet on the aortic velocity profiles. The same length was kept between the aortic inlet and the

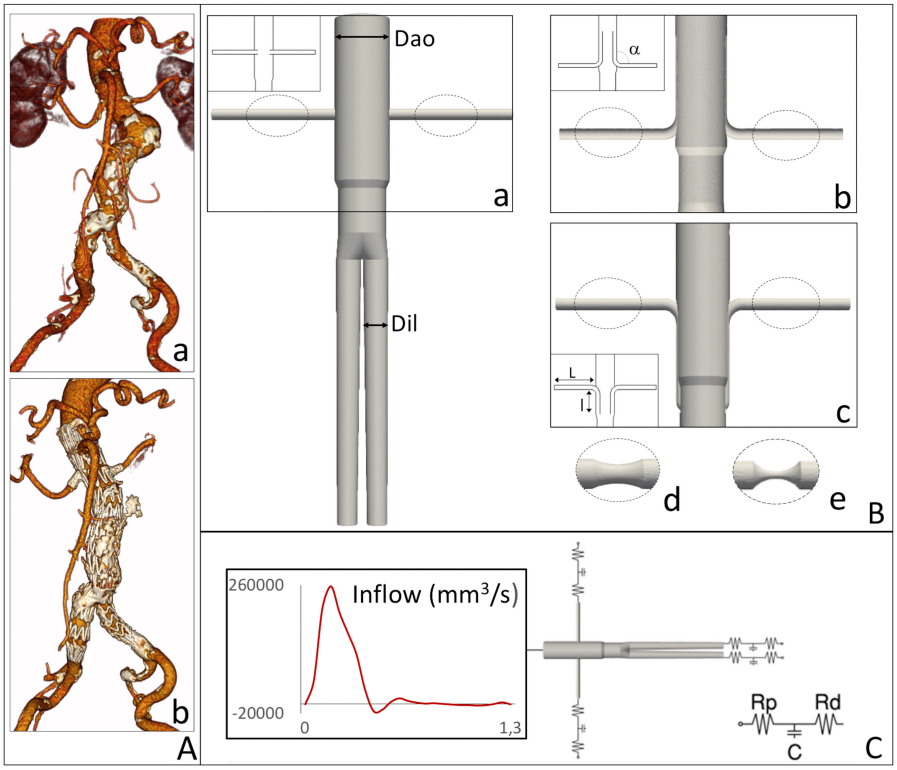

Figure 1.1. *A. 3D CT-scan view of abdominal aortic aneurysm non-eligible to conventional EVAR (a) and treated by fEVAR (b). B. Idealized model of fEVAR (a), chEVAR (b), and pEVAR (c) with sagittal slice view of each model in the black box. Surrounded by dashed lines, position of the 40%-diameter renal stenosis (d) and 70%-diameter renal stenosis (e) in the fEVAR, chEVAR and pEVAR models. C. Boundary conditions with patient-specific flow waveform applied at the aortic inlet, and the 3-element-windkessel model (proximal resistance (Rp), compliance (C) and distal resistance (Rd) at each outlet. Dao, aortic diameter (24 mm); Dil, iliac diameter (12 mm); α, angle of the renal chimney and renal periscope and between the aorta and the renal stentgraft in fEVAR (90°); L, length of the renal artery (62 mm); l, length of the vertical segment of the renal chimney and periscope (40 mm).*

	fEVAR	chEVAR	pEVAR	fEVAR -40	chEVAR -40	pEVAR -40	fEVAR -70	chEVAR -70	pEVAR -70
Aortic Inlet Systolic Pressure (mmHg)	166.2	148.7	148.3	167.5	150.2	148.7	187.8	170.7	169.5
Aortic Inlet Diastolic Pressure (mmHg)	70.9	73.6	72.9	70.7	73.3	71.5	74.3	76.4	76.1
Aortic Inlet Mean Pressure (mmHg)	94.2	93.7	92.8	94.3	93.7	91.8	102.0	101.4	100.7
Aortic Inlet Pulse Pressure (mmHg)	95.3	75.1	75.3	96.8	77.0	77.3	113.5	94.3	93.4
Renal Systolic Pressure (mmHg)	156.7	137.7	132.5	151.7	132.2	126.4	83.8	77.4	76.2
Renal Diastolic Pressure (mmHg)	71.2	74.3	73.4	70.9	74.0	72.0	63.4	65.9	65.0
Renal Mean Pressure (mmHg)	93.0	92.1	90.6	92.0	91.1	88.7	70.5	70.7	69.7
Renal Pulse Pressure (mmHg)	85.5	63.4	59.1	80.8	58.2	54.4	20.4	11.5	11.1
Iliac Systolic Pressure (mmHg)	156.0	141.4	141.4	156.8	142.8	141.4	174.0	160.8	159.9
Iliac Diastolic Pressure (mmHg)	71.6	74.5	73.6	71.3	74.2	72.2	75.0	77.5	77.0
Iliac Mean Pressure (mmHg)	93.4	92.9	92.1	93.4	92.9	91.1	100.9	100.4	99.6
Iliac Pulse Pressure (mmHg)	84.4	67.0	67.8	85.5	68.6	69.3	98.9	83.3	82.9
Renal Artery Maximal Velocity (mm/s)	1301.0	1564.3	1260.5	2099.7	2382.2	2347.2	5025.1	4971.5	4892.0
Mean Inflow (mm^3/s)	2.20	2.20	2.20	2.20	2.20	2.20	2.20	2.20	2.20

	fEVAR	chEVAR	pEVAR	fEVAR -40	chEVAR -40	pEVAR -40	fEVAR -70	chEVAR -70	pEVAR -70
Mean Renal outflow (mm^3/s)	0.29	0.29	0.29	0.29	0.29	0.29	0.22	0.22	0.22
Mean Iliac outflow (mm^3/s)	0.81	0.81	0.81	0.81	0.81	0.81	0.88	0.88	0.88
Prestenosis Renal Systolic Pressure (mmHg)	156.4	127.9	134.1	155.9	142.9	137.7	179.5	170.1	167.1
Prestenosis Renal Diastolic Pressure (mmHg)	71.0	73.9	73.3	70.8	73.8	73.6	74.2	76.4	76.1
Prestenosis Renal Mean Pressure (mmHg)	92.4	90.6	90.9	92,3	92.5	91.5	100.4	100.9	100.0
Prestenosis Renal Pulse Pressure (mmHg)	85.3	54.1	60.8	85.1	69.2	64.1	105.2	93.7	91.0
Poststenosis Renal Systolic Pressure (mmHg)	156.1	127.9	133.6	146.6	127.9	124.1	82.6	77.1	76.0
Poststenosis Renal Diastolic Pressure (mmHg)	71.1	73.9	73.3	70.8	73.9	73.7	63.2	65.6	64.8
Poststenosis Renal Mean Pressure (mmHg)	92.3	90.6	90.8	90.9	90.6	89.7	69.9	70.3	69.4
Poststenosis Renal Pulse Pressure (mmHg)	85.1	54.1	60.2	75.7	54.1	50.5	19.4	11.5	11.2

Table 1.2. *Pressure and flow values at inlet and outlets in all idealized models. fEVAR, fenestrated EVAR; chEVAR, chimney EVAR; pEVAR, periscope EVAR; -40 , 40% stenosed renal arteries; -70 , 70%-stenosed renal arteries.*

proximal end of the renal stentgraft in order to have an established flow. In the fEVAR model, renal stents were aligned to the renal ostium and protruded 5 mm into the aortic lumen. In pEVAR and chEVAR, the renal stent protruded 40 mm vertically into the aortic lumen. The angle between the renal artery segment of the stent graft and its aortic segment was 90Â°. An image of each model is shown in Figure 1.1. CFD analyses were performed using the validated finite element code CRIMSON (from: http://www.crimson.software/ (n.d.)) on the high performance computer of Mines Saint-Etienne (cluster of 11 Tflops with 26 nodes totaling 384 cores and 1Tb of RAM). Tetrahedral mesh was created by discretizing the geometric model of the aorta and refined using a combination of global mesh, maximum curvature and boundary layers refinement. Pulsatile flow was run, followed by iterative field-based anisotropic refinement operation until mesh independent results were obtained (Sahni *et al*. (2006), Youssefi *et al*. (2018)). Mesh independency was assessed for each model in all patient. The results of the inlet and outlet pressures were compared between each mesh adaptation of the same model. Mesh adaptivity was stopped when the differences in inlet and outlet pressures between two consecutive mesh adaptations was below 1%. Two mesh adaptations were performed in order to reach mesh independency. Mesh sizes ranged between 0.6×106 and 2.4×106 elements. The vessel and stentgraft walls were modeled as rigid. The blood was treated as a Newtonian and incompressible fluid with a dynamic viscosity of 4 mPa.s and a density of 1060 kg/m^3. A liquid is said to be Newtonian if the coefficient of viscosity is constant at all rates of shear. This condition exists in most homogeneous liquids, including blood plasma (which, since it consists of mostly water, is Newtonian). But the mechanical behavior of a liquid containing a suspension of particles (like blood) can vary such that the liquid becomes non-Newtonian. These deviations become particularly significant when the particle size becomes appreciably large in comparison to the dimension of the channel in which the fluid is flowing. In the large vessels, such as aorta, iliac and renal arteries, it is reasonable to assume blood has a constant viscosity, because the vessel diameters are large compared with the individual cell diameters, and because shear rates are high enough for viscosity to be independent of them. Hence, in these vessels the non-Newtonian behavior becomes insignificant and blood can be considered to be a Newtonian fluid (Ottesen *et al*. (2004)). A pulsatile adapted patient specific flow waveform (Ahmed *et al*. (2016)) was prescribed at the aortic inlet using a Womersley velocity profile (Williams and Leggett (1989), Odenstedt *et al*. (2001), Osinnski *et al*. (1995)). The flow fraction that feeds the supra-aortic trunks and the digestive arteries was removed from the cardiac outpout (4 L/min) and the adapted aortic inflow represented 55% of the cardiac output (2.2 L/min). Outflow boundary conditions were prescribed using a coupled-multi-domain method (Vignon-Clementel *et al*. (2006), Figueroa *et al*. (2006)) in which 3-element-Windkessel models were coupled to each outflow branch (renal and iliac arteries) (Vignon-Clementel *et al*. (2010)). The Windkessel model represents the arterial tree beyond the outlet in an intuitive and physiological manner. It comprises of a proximal resistance, compliance, and a distal resistance for each

outlet. Specification of the Windkessel parameters requires knowledge of flow splits and pressure (Sahni *et al*. (2006)). The prescribed mean, systolic, and diastolic aortic pressures were 93.3 mmHg, 120 mmHg and 80 mmHg, respectively (Figure 1.1). The Windkessel parameters for outlets were estimated following the procedure described in (Xiao *et al*. (2014)) paper and are summarized in Table 1. The inflow waveform and the outlet boundary condition parameters were kept constant in all cases for the sake of comparison. Simulations were run until a periodic solution was achieved, imposing total residual tolerance criterion (sum of all nodal residuals) of 10^{-3}. Only the results of the last cardiac cycle are reported. For each model, systolic pressure (SP), diastolic pressure (DP), mean pressure (MP), pulse pressure (PP) and mean flow (Qm) were measured at aortic inlet, all model outlets, and the proximal and distal segments of the renal arterial stenosis. Time averaged WSS (TAWSS) and platelet activation state (PAS) were determined in the renal arteries and in the renal stents. Peak velocities were also measured 3 cm downstream the renal artery ostium, i.e. at the end of the stenosis for the stenosed models. Platelet activation state was calculated for each case according to the validated Lagrangian-based model of shear induced platelet activation proposed by (Grigioni *et al*. (2005)), adapted by (Nobili *et al*. (2008)) and applied to the carotid artery by (Massai *et al*. (2012)). PAS is a dimensionless parameter. It aimed to evaluate the hemodynamic risk related to platelet activation and aggregation, that increase the risk for thromboembolic complications (Massai *et al*. (2012)). Pressures, flows, velocities, TAWSS and PAS were compared between non-stenosed and stenosed models.

1.3. Results

Since all geometric models are symmetrical, pressure, flow and velocity values were identical in the left and right renal arteries. Thus only the results for the left renal artery were reported. Numerical values for flow, velocity and pressure obtained are listed in Table 2.

1.3.1. *Model without stenosis*

1.3.1.1. *Flow and velocity*

Qm at aortic inlet, at renal outlets (0.6L/min) and at iliac outlets (1.6 L/min) were the same in all idealized models. The largest renal artery velocity (3cm after the renal ostium), was found in chEVAR (1.6 m/s). In the same region, the peak velocity for pEVAR and fEVAR was 18% lower (Figure 1.2). Flow recirculation, indicating vortex formation, was found at the proximal intra renal cranial part of the fenestrated stentgraft and in the aortic segment located just below the fenestrated stentgraft as well as at the entrance of the periscope stentgraft as represented in Figures 1.3 and 1.4.

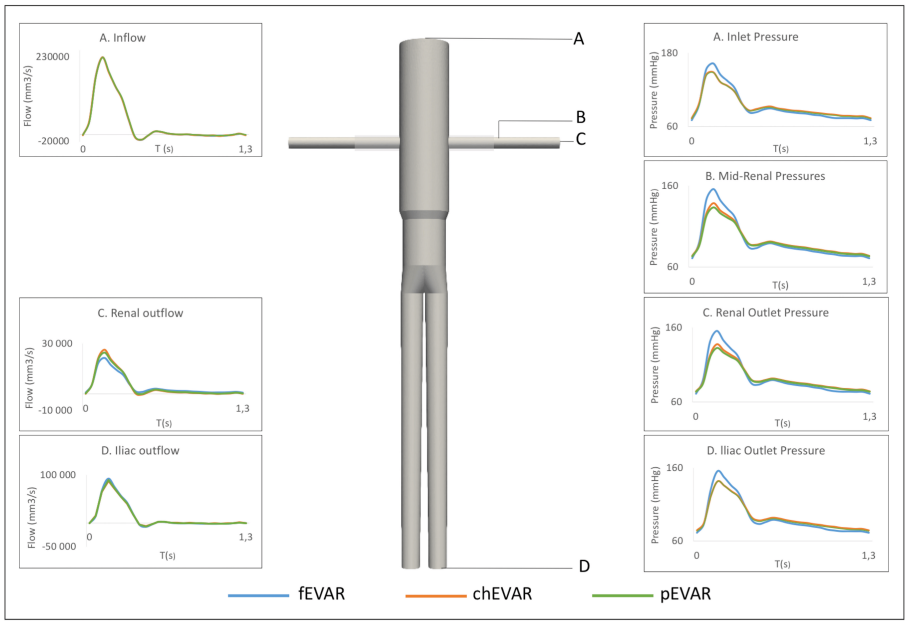

Figure 1.2. *Flows and pressures at aortic inlet (A), mid-renal artery (B), renal artery outlet (C) and iliac artery outlet (D) in the baseline models (without stenosis). We chose to report only the results of the left renal artery and the left iliac artery as the models were symmetric and the results of the contralateral side were the same.*

1.3.1.2. *Pressure*

Aortic inlet SP and PP were 11% and 21% higher in fEVAR compared to chEVAR and pEVAR, respectively. MP were almost identical in all cases, around 93.5 mmHg. SP at renal arteries were 12% and 15% higher in fEVAR compared to chEVAR and pEVAR, respectively. PP in renal arteries were 26% and 31% higher in fEVAR compared to chEVAR and pEVAR, respectively. DP ranged between 71 mmHg and 74 mmHg. MP was nearly identical in all cases, around 92 mmHg.

1.3.1.3. *Renal artery WSS and PAS*

As represented in Figure 1.5, TAWSS was the lowest (< 0.4 Pa) at the proximal intra renal segment of the fenestrated stent graft in fEVAR, and at the proximal horizontal segment of the chimney and periscope stent grafts. The TAWSS peak values (> 7 Pa) were reached at the proximal aortic end of the fenestrated stent graft, and at the proximal vertical segment and at the curvature of the chimney stentgraft and at the proximal vertical part of periscope stentgraft. PAS is represented in Figure

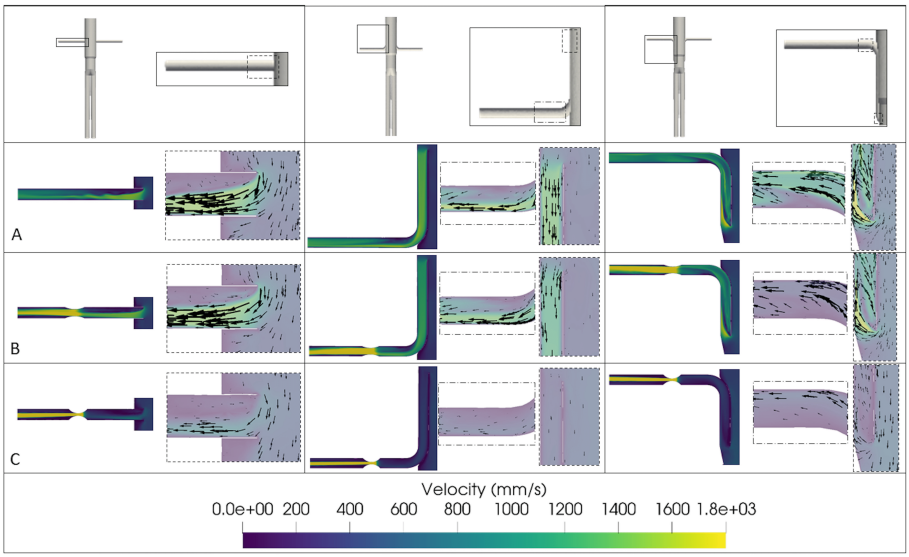

Figure 1.3. *Velocity field in the renal arteries of the idealized models (surrounded by solid lines) without renal stenosis (A), with 40%-diameter renal stenosis (B) and with 70%-diameter renal stenosis at peak systole. Surrounded by dashed lines, zoom of the proximal part of the stentgraft (fenestrated, chimney and periscope) and the horizontal portion of chimney and periscope stent-graft.*

1.6. At systolic peak, PAS was the highest in the horizontal part of the periscope stentgraft and in the renal artery in pEVAR. PAS was the lowest at the proximal part of the renal chimneys in chEVAR. The highest value for PAS in fEVAR was 0.01 and was found in the fenestrated stentgraft and in the renal artery. The highest value of PAS in chEVAR was 0.0036, located at the renal stent angulation, the distal part of the chimney and the renal artery. The highest value for PAS in pEVAR was 0.02 and was found in distal part of the periscope stent-graft and in the renal artery.

1.3.2. *Model with 40%-diameter stenosis*

1.3.2.1. *Flow and velocity*

Qm in renal and iliac arteries were identical for all three cases. This suggests that the renal artery stenosis has a larger impact on flow dynamics than the different effective resistances to flow set by the different renal stentgraft configurations. Larger velocities resulting from the stenoses were recorded in the renal arteries. Peak velocity at the renal artery (3cm after the renal ostium) was almost identical in chEVAR-40 and

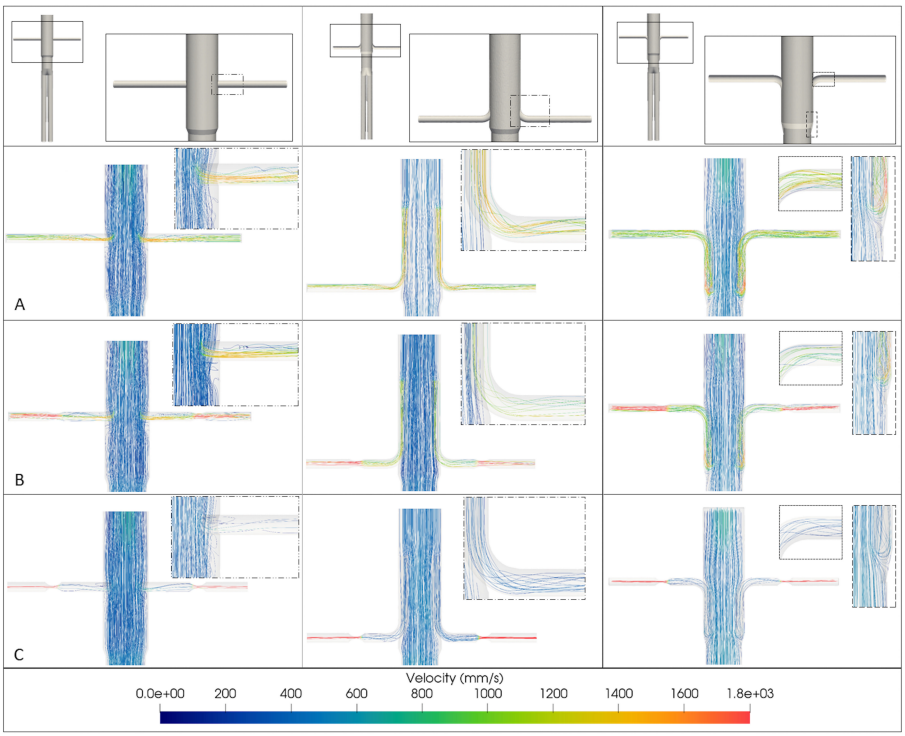

Figure 1.4. *Velocity streamlines in each idealized model (solid lines) without renal stenosis (A), with 40%-diameter renal stenosis (B) and with 70%-diameter renal stenosis at peak systole. Surrounded by dashed lines, detailed view in portion of the model with complex flow streamlines.*

pEVAR-40 (2.38 m/s and 2.35 m/s) and 12%-lower in fEVAR-40, as represented in Figure 1.7. Flow recirculation was found in the aortic segment distal to the fenestrated stentgraft and at the proximal intrarenal part of the fenestrated stentgraft, as well as at the entrance of the periscope stentgraft as can be represented in Figures 1.3 and 1.4.

1.3.2.2. *Pressures*

As can be represented in Figure 1.8, the variations of pressures (SP, PP, DP, MP) at the renal and iliac outlets were identical to the baseline models (without stenosis). Aortic inlet SP and PP were higher in fEVAR compared to chEVAR and pEVAR, respectively. MP were almost identical in all cases, around 93.3 mmHg. SP at renal arteries were higher in fEVAR compared to chEVAR and pEVAR. PP in renal arteries were around 30% higher in fEVAR compared to chEVAR and pEVAR, respectively.

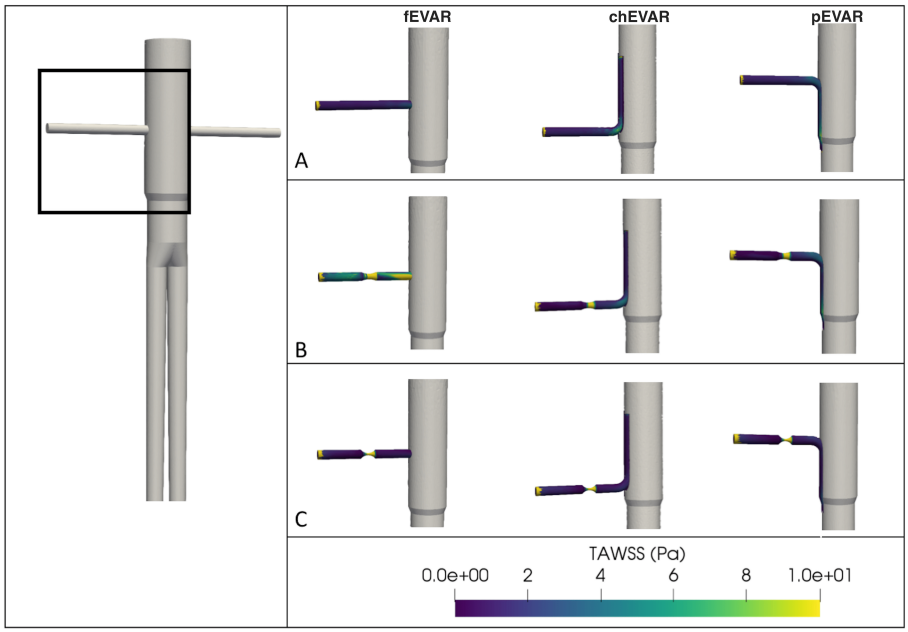

Figure 1.5. *TAWSS in the renal arteries of the idealized models (solid lines) without renal stenosis (A), with 40%-diameter renal stenosis (B) and with 70%-diameter renal stenosis at peak systole.*

DP ranged between 71 mmHg and 74 mmHg. MP ranged between 89 and 92mmHg. Pre and poststenosis SP and PP were higher in fEVAR-40 compared to chEVAR and pEVAR. The MP drop in renal stenosis was identical in all 40% stenosed models : 2%. The SP drop in renal stenosis was 6 % in fEVAR-40 and 10% in chEVAR and pEVAR. The PP drop in renal stenosis was 11% in fEVAR-40 and 21% in chEVAR and pEVAR. Pre and post-renal stenosis DP were similar in all models.

1.3.2.3. *WSS and PAS in renal arteries*

As represented in Figure 1.5, TAWSS was the lowest ($<$ 0.4 Pa) in the post-stenotic renal artery in all models. Low TAWSS values occurred also in the cranial segment of the proximal intrarenal part of the fenestrated stentgraft, in the cranial segment of the proximal horizontal part of the chimney and at the caudal segment of the proximal horizontal part of the periscope. TAWSS was the highest (around 15 Pa) at the proximal part of the renal stenosis in all models followed by the proximal vertical part of pEVAR-40 (around 7 Pa). TAWSS was moderate (around 4 Pa) in the angulation of pEVAR-40 and chEVAR-40. PAS is represented in Figure 1.6. At systolic peak, the highest value for PAS was found in chEVAR-40 and the lowest

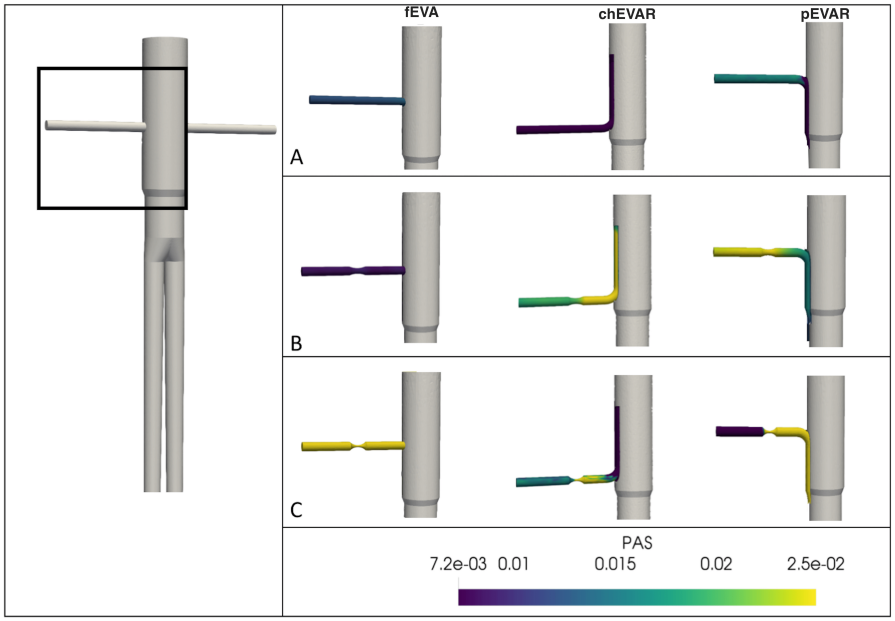

Figure 1.6. *PAS in the renal arteries of the idealized models (solid lines) without renal stenosis (A), with 40%-diameter renal stenosis (B) and with 70%-diameter renal stenosis at peak systole.*

in fEVAR-40. Highest PAS value in fEVAR-40 was 0.009 at the renal stenosis. The highest value of PAS in chEVAR-40 was 0.032 and located above the renal artery stenosis to the proximal part of the chimney stentgraft. The highest value of PAS in pEVAR-40 was 0.025 and was found from the stenosis to the end of the renal artery. Compared to the baseline models, the values of PAS in fEVAR-40 and pEVAR-40 remained relatively constant. However, PAS in the chEVAR-40 increased by almost ten times.

1.3.3. *Model with 70%-diameter stenosis*

1.3.3.1. *Flow and velocity*

Qm in renal and iliac arteries were identical for all three cases. Renal artery flows were 24%-lower than in the non-stenosed models. As show in Figure 1.7, peak velocity was similar (around 5 m/s) in all 3 models. Flow recirculation was present at the proximal part of the fenestrated stentgraft and at the aortic segment located just

below the fenestrated stentgraft as well as at the entrance of the periscope stentgraft as can be represented in Figures 1.3 and 1.4.

1.3.3.2. *Pressures (Figure 1.8)*

Aortic inflow pressure noticeable increased in all models (PP increases relative to the non-stenosis models of 13%, 15%, and 14% for fEVAR, chEVAR and pEVAR, respectively). This clearly indicates that a larger pressure is needed to drive the same amount of flow in the presence of the hemodynamically-significant renal stenoses. fEVAR SP at the renal arteries was approximately 9% larger than chEVAR-70 and pEVAR-70. Renal PP was around 44% higher in fEVAR-70 compared to chEVAR-70 and pEVAR-70. Renal DP ranged between 63 and 66 mmHg. Renal MP were similar in all models, around 70 mmHg. Pre- and post-renal stenosis SP and PP were higher in fEVAR-70 compared to chEVAR and pEVAR. The pressure drop in the renal stenosis was identical in all models: around 54% for the SP, 15% for the DP, 31% for the MP and 86% for the PP.

1.3.3.3. *TAWSS and PAS in renal arteries*

As represented in Figure 1.5, TAWSS was the highest (around 100 Pa) at the renal stenosis in all models. TAWSS was the lowest ($<$0.4 Pa) at the post-stenotic renal artery in all models and at the cranial intrarenal segment of the fenestrated stentgraft as well as at the caudal intrarenal segment of the horizontal part of the periscope. PAS is represented in Figure 1.6. Compared to the baseline models, the values of PAS in the 70%-stenosed models increased. At systolic peak, the highest value for PAS was found in pEVAR-70. The highest value for PAS in pEVAR-70 was 0.078 located above the stenosis (angulation and proximal vertical part of the periscope stent-graft). The highest PAS value in chEVAR-70 was 0.034 located from the proximal part of the stenosis to the angulation of the chimney stentgraft. The highest PAS in fEVAR-70 was 0.052 located between the stenosis and the end of the renal artery.

1.4. Discussion

The use of complex EVAR has expanded in recent years. As fenestrated, chimney and periscope stentgrafts protrude into the aortic lumen, these complex endovascular repairs could potentially interfere with the renal blood flow. One of the most serious complication is intimal hyperplasia, responsible for narrowing and occlusion of the target vessel, that can lead to organ ischemia. Platelet activation is one of the mechanisms involved in this phenomenon. High shear stress can stimulate platelet activation, aggregation and lytic process, whereas low shear stress leads to endothelium damage, atherosclerosis, and intimal hyperplasia (Massai *et al*. (2012)). Understanding the hemodynamic impact of fEVAR, ChEVAR and pEVAR configurations on renal arteries, as well as the impact of renal stenosis could help the physician to choose the best endovascular option for each patient. Only a few studies

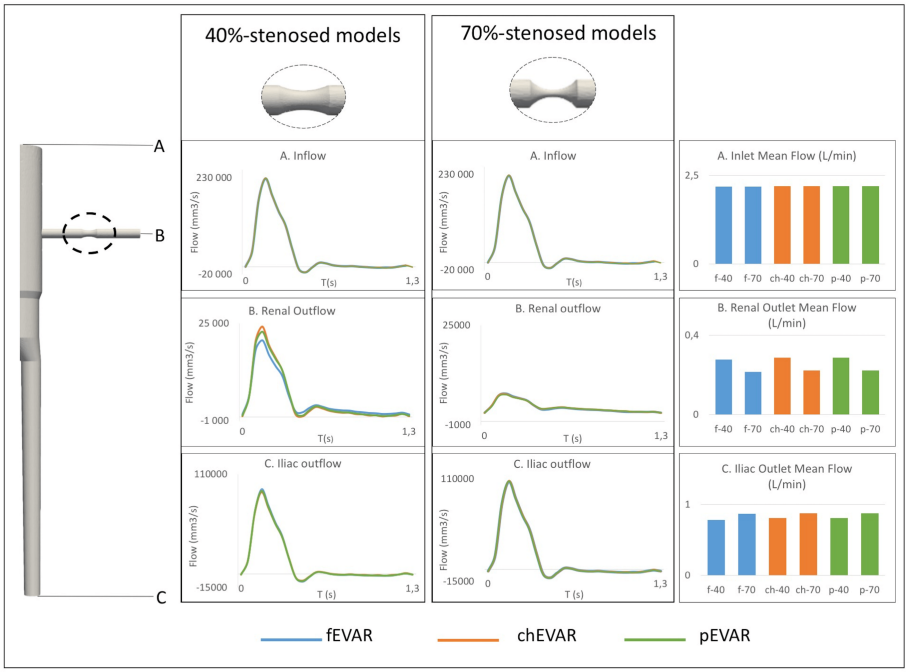

Figure 1.7. *Flow waveforms and mean flow bar charts at aortic inlet (A), renal artery outlet (B), and iliac artery outlet (C) of the 40% and 70%-renal artery stenosed models for the last cardiac cycle. The renal stenosis is surrounded by dashed lines in the model on the left. The results of the 40%-stenosed models and 70%-stenosed models are reported in 2 columns. The flow waveforms of the 40%-stenosed fEVAR, chEVAR and PEVAR are reported on the first column. The flow waveforms of the 70%-stenosed fEVAR, chEVAR and PEVAR are reported on the second column. Mean flow of the 40%-stenosed fEVAR (f-40), 40%-stenosed chEVAR (ch-40), 40%-stenosed pEVAR (p-40), 70%-stenosed fEVAR (f-70), 70%-stenosed chEVAR (ch-70), 70%-stenosed pEVAR (p-70) are reported in bar charts on the last column. We chose to report only the results of the left renal artery and the left iliac artery as the model was symmetric and the results of the contralateral side were the same.*

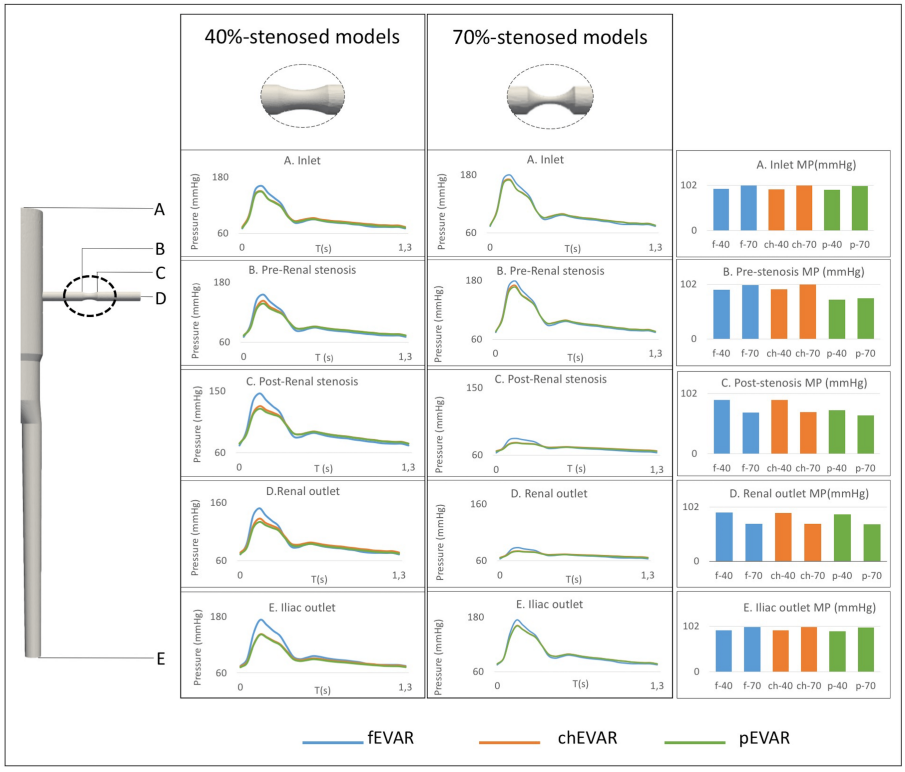

Figure 1.8. *Pressure waveforms and mean pressure bar charts at aortic inlet (A), pre-renal stenosis (B), post-renal stenosis (C), renal artery outlet (D), and iliac artery outlet (E) of the 40% and 70%-renal artery stenosed models. The renal stenosis is surrounded by dashed lines in the model on the left. The results of the 40%-stenosed models and 70%-stenosed models are reported in 2 columns. The pressure waveforms of the 40%-stenosed fEVAR, chEVAR and PEVAR are reported on the first column. The pressure waveforms of the 70%-stenosed fEVAR, chEVAR and PEVAR are reported on the second column. Mean pressure of the 40%-stenosed fEVAR (f-40), 40%-stenosed chEVAR (ch-40), 40%-stenosed pEVAR (p-40), 70%-stenosed fEVAR (f-70), 70%-stenosed chEVAR (ch-70), 70%-stenosed pEVAR (p-70) are reported in bar charts on the last column. We chose to report only the results of the left renal artery and the left iliac artery as the model was symmetric and the results of the contralateral side were the same.*

in the literature have analyzed renal artery flow and pressure patterns following complex endovascular interventions. A close computational study published by (Kandail *et al*. (2015)) compared blood flow in chEVAR, pEVAR and fEVAR. The originality of our approach compared to this previous study is the introduction of a renal artery stenosis in these endovascular repairs of complex aortic aneurysm, and the comparison of the pressure, flow, TAWSS and PAS between the models. No studies have analyzed the hemodynamic impact of renal artery stenosis in idealized models of complex aortic aneurysm endovascular repairs. Abnormal flow and shear stress are involved in the occurrence of intimal hyperplasia. Following stent implantation, the stented segment of the artery can be stenosed by four key processes: thrombus formation, arterial inflammation, neointimal hyperplasia and remodeling. Neointimal hyperplasia appears within the weeks after stent implantation followed by remodeling. Smooth muscle cells which normally sit in the middle layer of the artery migrate inwards towards the stent where they proliferate and form the bulk of the new tissue that narrows the artery. The migration and proliferation of smooth muscle cells is triggered by various chemical signals such as injured endothelial cells, dysfunctional endothelial cells, activates platelets at the site of arterial injury. Abnormal hemodynamics near the stent result in altered stresses on the endothelial cells and potential mechanical activation of platelets. Then collagen deposits in the outer layer of the artery leads to arterial stiffening. This process increases the pressure onto the stent and can squeeze the arterial wall between inter-strut spaces (Murphy and Boyle (2010)). Stent implantation under low flow is associated to increased neointima formation (Richter *et al*. (1999)). Tissue growth in stented artery is prominent at the site of low WSS (< 0.5 Pa) (LaDisa Jr *et al*. (2005)).

1.4.1. *Velocity and flow*

Total renal blood flow usually accounts for 15 to 20% of the cardiac output under normal resting conditions (Williams and Leggett (1989), Moore Jr and Ku (1994)). Our total renal blood flow was physiologic as it represented 15% of the cardiac output (Weinstein and Anderson (2010)). The stenosed geometries (both 40% and 70%) showed no noticeable differences in renal flow between the different renal stent designs. (Šutalo *et al*. (2008)) observed negligible difference in the outflow rates to a branch vessel in antegrade and retrograde directions for 40-mm long conduits in his experimental study. For the baseline (without stenosis) geometry, the chEVAR design resulted in the largest peak velocity in renal arteries. This result is in agreement with (Kandail *et al*. (2015)) in his computational study. The larger the renal artery stenosis the lesser the flow recirculation in the aortic segment located just below the fenestrated stentgraft and at the entrance of the periscope stentgraft. No vortical structures were observed in the set of chEVAR models. However, they were observed in all fEVAR and pEVAR models.

1.4.2. *Pressure*

The fEVAR design resulted in the largest pulse and systolic pressures for all idealized anatomical models. This finding suggests that this design induces the largest viscous losses in the abdominal region. Under the assumption that the aortic flow is maintained, higher viscous losses result in the largest pressures seen in the fEVAR design. The renal artery stenosis impacted the hemodynamics in all models. In clinical practice, renal artery stenosis have hemodynamic impact when they reach 50% of the diameter and they have a clinical impact when they reach 70% of the diameter (Lao *et al*. (2011), Li *et al*. (2008)). In the 40% stenosis models, negligible pressure variations were found before and after the stenosis. However, in the 70% renal stenosis models, significant pressure drops were observed, confirming the important hemodynamic impact of a 70%-stenosis in the renal artery. At the aortic inlet, systolic, mean and pulse pressures were higher in fEVAR whatever the stenosis degree was. Pre- and post-stenosis renal artery pressures were also higher in fEVAR whatever the stenosis degree was. This could be related to the increase of resistance in the fenestrated renal artery as the flow makes a 90° angulation before entering into the fenestrated renal stent that protrudes into the aortic lumen. Pulse pressure was reported as this parameter has an important role in remodeling, wall thickening and stiffening (Eberth *et al*. (2009)). FEVAR had the highest PP whatever the degree of stenosis, meaning that it presents the highest risk of remodeling and wall thickening for the renal artery.

1.4.3. *TAWSS*

Low WSS values correlate with intimal hyperplasia and in-stent stenosis whereas high WSS with endothelial damage. Low shear stress was found below and above the 40% and the 70%-stenosis. Moderate TAWSS values were found in the following regions: proximal end of the fenestrated renal stentgraft, angulation of the renal chimney stentgraft, vertical ascending part and angulation of the renal periscope stentgraft. These results corroborate the study of (Suess *et al*. (2016)). Low TAWSS was found at the intra-renal proximal cranial segment of the fenestrated stentgraft. Its configuration at the aortic inlet requires a 90° change of direction of the flow momentum that results in separation of the flow and vortices. Recirculation and downstream flow were observed in the cranial extent of the proximal part of the renal stent, and this can lead to the development of intimal hyperplasia. However, the artery is not exposed to this phenomenon as the stentgraft is usually covered, hence protecting the artery (Suess *et al*. (2016)). Regarding flow recirculation, it seems to be more important during peak respiratory motion, that can reach 3 mm displacement at the proximal and distal ends of the renal artery. However, in fEVAR, the motion of the proximal and distal ends of the renal artery are reduced by 25 and 80% respectively (Muhs *et al*. (2008)). The fixation of the proximal part of the stentgraft in the main body allows motion of the distal part of the stentgraft that can lead to

intimal hyperplasia (Suess *et al*. (2016)). Chimneys are usually further extended in the renal artery than in fEVAR, where the renal artery can move to a larger extent (Ullery *et al*. (2016)), and this can lead again to an increased risk of intimal hyperplasia. In chEVAR, the antegrade part of the stent decreases flow disturbance. In the angulation, the changes of direction lead to oscillations and high WSS. The same trend as in fEVAR was observed in the cranial extent of the proximal entrance of the chimney in the renal artery. The periscope has a retrograde configuration with a takeoff angle that makes 180° to reach the lateral part of the periscope. The flow is dramatically disturbed at the proximal end of the periscope with oscillating flow and high WSS, that can lead to endothelial damage and thrombosis. At the angulation of the periscope, the trend was the same as in chEVAR but with less flow disturbance and moderate TAWSS. The TAWSS was low in the caudal extent of the proximal entrance of the periscope in the renal artery. The largest vortical structures were found at the cranial segment of the proximal part of the fenestrated stentgraft and in the part of the main stent graft that was located below the renal fenestrated stentgraft where TAWSS was < 0.4.

1.4.4. *PAS*

Thrombus formation was not simulated directly in this study, but PAS was used to identify regions with a high risk of thrombosis. These metrics were used to quantify the history of shear experienced by massless particles moving through the vasculature. This tool can be used to compare the performance of different endograft designs on a patient-specific basis (Massai *et al*. (2012)). The impact of the renal stenosis was more important in fEVAR with a higher increase of PAS between the non-stented and the 70%-diameter renal stenosis at systolic peak. In the 70% stenosed models, platelets were exposed to high shear stress for a short time due to the flow acceleration in the stenosis. Platelets were more fastly activated in fEVAR, followed by pEVAR and chEVAR. In the 40% renal stenosis models, platelets were more fastly activated in the proximal part of chEVAR and in the distal part of the renal artery in pEVAR. In the models without stenosis, platelets were more activated in the renal artery and in the part below the angulation of the periscope stentgraft. Platelets were less activated in chEVAR. Platelets were activated above both stenoses in chEVAR, and 70%-stenosis in pEVAR. The physiological range of wall shear stress varies from 0.1 and 6 Pa, higher values activating platelets. Potential change from low to high shear induces platelets activation and thrombus formation (Holme *et al*. (1997)), which can explain the increased platelet activation in the stenosis. The chEVAR configurations revealed a smoother shear stress distribution along the renal branches, which predispose to less material fatigue or a lower trend for renal events in long-term. In practice, chimneys have less acute angulations compared to fEVAR bridging stent (Georgakarakos *et al*. (2015)). The effect of the stenosis on pressure and velocity was more important in the fEVAR, followed by pEVAR with highest PAS at systolic peak value in the non-stenosed and 70% stenosed models. fEVAR

seems to be more sensitive to the occurrence and narrowing of a renal stenosis. In the non-stenosed models, chEVAR had the lowest value of PAS, followed by pEVAR and fEVAR. In the 40%-stenosed models, fEVAR-40 had the lowest value of PAS, followed by chEVAR-40 and pEVAR-40. In the 70%-stenosed models, chEVAR-70 had the lowest value of PAS followed by fEVAR-70 and pEVAR-70.

1.4.5. *Limitations*

Several assumptions were taken in this study. The walls were assumed rigid. However, the material of the stentgrafts has low compliance. The results of CFD-simulations can be highly coupled to boundary conditions used in the computed analysis. Only one geometry of fEVAR, chEVAR and pEVAR was analyzed in our study. Many geometries need to be analyzed in further studies. (Georgakarakos *et al*. (2015)) showed that the lowest value of WSS was found for 90° whereas the highest at 45°. Geometry was idealized in our analysis. Further study will be achieved on patient specific models (specific anatomy and specific physiology). The study was focused on WSS and PAS but other criteria, including material fatigue, could be relevant to predict risks such as intimal hyperplasia or thrombosis. All models represented an idealized geometry and allowed to run sensitivity analyses without effects of interindividual variations of anatomy. All geometric models, in addition of being idealized, have also neglected aortic curvature. Stented abdominal aneurysms typical have tortuosity in the coronal and sagittal directions, which can significantly affect the hemodynamics (Figueroa *et al*. (2009)). Lastly, the effect of renal autoregulation in response to alterations in flow was not included. With the modeling approach presented here, the Windkessel parameters were kept constant for all geometric models. This fundamentally means that the distal resistance of the kidney vascular bed was assumed to not respond to a situation for reduced flow such as that observed in the 70% renal stenosis geometry. In reality, alterations in renal flow and pressure would trigger the renin-angiotensin-aldosterone response (Textor and Lerman (2015)). However, a given renal artery stenosis can generate widely variable hemodynamic effects in different patient. Mounier-Vehier et al. observed significant increase of renal blood flow after angioplasty of renal artery stenosis in hypertensive patients (Mounier-Vehier *et al*. (2004)) which means that renal artery stenosis decreased renal blood flow in these symptomatic patients.

1.5. Conclusion

Computational fluid dynamics is a powerful tool that enabled us to compare systematically the hemodynamics patterns obtained after different types of complex EVAR procedures and for different degrees of possible renal stenosis. Hemodynamics alterations seem to be more significant in fEVAR in presence of renal stenosis. The fEVAR model seems to carry higher risk of thrombosis. The chEVAR

and pEVAR seem to induce less hemodynamics alterations but carry higher risk of thrombosis in presence of a renal stenosis. However our findings in idealized models has to be validated in anatomical models. Further studies with patient specific analyses need to be performed as it is now evident that complex EVAR have a major hemodynamical impact which needs to be considered in the treatment of complex abdominal aortic aneurysms.

1.6. Acknowledgements

SA is grateful to the European Research Council (ERC grant Biolochanics, grant number 647067) for financial support.

1.7. Bibliography

Ahmed, S. B., Dillon-Murphy, D., Figueroa, C. (2016), Computational study of anatomical risk factors in idealized models of type b aortic dissection, *European Journal of Vascular and Endovascular Surgery*, 52(6), 736–745.

Draney, M. T., Zarins, C. K., Taylor, C. A. (2005), Three-dimensional analysis of renal artery bending motion during respiration, *Journal of Endovascular Therapy*, 12(3), 380–386.

Eberth, J. F., Gresham, V. C., Reddy, A. K., Popovic, N., Wilson, E., Humphrey, J. D. (2009), Importance of pulsatility in hypertensive carotid artery growth and remodeling, *Journal of hypertension*, 27(10), 2010.

Figueroa, C. A., Taylor, C. A., Yeh, V., Chiou, A. J., Zarins, C. K. (2009), Effect of curvature on displacement forces acting on aortic endografts: a 3-dimensional computational analysis, *Journal of Endovascular Therapy*, 16(3), 284–294.

Figueroa, C. A., Vignon-Clementel, I. E., Jansen, K. E., Hughes, T. J., Taylor, C. A. (2006), A coupled momentum method for modeling blood flow in three-dimensional deformable arteries, *Computer methods in applied mechanics and engineering*, 195(41-43), 5685–5706.

from: http://www.crimson.software/, A. (n.d.), 'Cardiovascular integrated modelling and simulation (crimson).'.

Georgakarakos, E., Manopoulos, C., Lazarides, M. K., Tsangaris, S. (2015), Commentary: occlusion of parallel/bridging stent-grafts in the treatment of complex aneurysms: a purely technical issue... or not?, *Journal of Endovascular Therapy*, 22(3), 401–405.

Grigioni, M., Morbiducci, U., D'Avenio, G., Di Benedetto, G., Del Gaudio, C. (2005), A novel formulation for blood trauma prediction by a modified power-law mathematical model, *Biomechanics and Modeling in Mechanobiology*, 4(4), 249–260.

Holme, P. A., Ørvim, U., Hamers, M. J., Solum, N. O., Brosstad, F. R., Barstad, R. M., Sakariassen, K. S. (1997), Shear-induced platelet activation and platelet microparticle formation at blood flow conditions as in arteries with a severe stenosis, *Arteriosclerosis, thrombosis, and vascular biology*, 17(4), 646–653.

Kandail, H., Hamady, M., Xu, X. Y. (2015), Comparison of blood flow in branched and fenestrated stent-grafts for endovascular repair of abdominal aortic aneurysms, *Journal of Endovascular Therapy*, 22(4), 578–590.

LaDisa Jr, J. F., Olson, L. E., Molthen, R. C., Hettrick, D. A., Pratt, P. F., Hardel, M. D., Kersten, J. R., Warltier, D. C., Pagel, P. S. (2005), Alterations in wall shear stress predict sites of neointimal hyperplasia after stent implantation in rabbit iliac arteries, *American Journal of Physiology-Heart and Circulatory Physiology*, 288(5), H2465–H2475.

Lao, D., Parasher, P. S., Cho, K. C., Yeghiazarians, Y. (2011), Atherosclerotic renal artery stenosis–diagnosis and treatment, *in* Mayo Clinic Proceedings, vol. 86, Elsevier, pp. 649–657.

Li, J.-c., Jiang, Y.-x., Zhang, S.-y., Wang, L., Ouyang, Y.-s., Qi, Z.-h. (2008), Evaluation of renal artery stenosis with hemodynamic parameters of doppler sonography, *Journal of vascular surgery*, 48(2), 323–328.

Martin-Gonzalez, T., Pinçon, C., Hertault, A., Maurel, B., Labbé, D., Spear, R., Sobocinski, J., Haulon, S. (2015), Renal outcomes analysis after endovascular and open aortic aneurysm repair, *Journal of vascular surgery*, 62(3), 569–577.

Massai, D., Soloperto, G., Gallo, D., Xu, X. Y., Morbiducci, U. (2012), Shear-induced platelet activation and its relationship with blood flow topology in a numerical model of stenosed carotid bifurcation, *European Journal of Mechanics-B/Fluids*, 35, 92–101.

Mohabbat, W., Greenberg, R. K., Mastracci, T. M., Cury, M., Morales, J. P., Hernandez, A. V. (2009), Revised duplex criteria and outcomes for renal stents and stent grafts following endovascular repair of juxtarenal and thoracoabdominal aneurysms, *Journal of vascular surgery*, 49(4), 827–837.

Moore Jr, J. E., Ku, D. N. (1994), Pulsatile velocity measurements in a model of the human abdominal aorta under resting conditions, , .

Mounier-Vehier, C., Cocheteux, B., Haulon, S., Devos, P., Lions, C., Gautier, C., Carre, A., Beregi, J.-P. (2004), Changes in renal blood flow reserve after angioplasty of renal artery stenosis in hypertensive patients, *Kidney international*, 65(1), 245–250.

Muhs, B. E., Vincken, K. L., Teutelink, A., Verhoeven, E. L., Prokop, M., Moll, F. L., Verhagen, H. J. (2008), Dynamic cine-computed tomography angiography imaging of standard and fenestrated endografts: differing effects on renal artery motion, *Vascular and endovascular surgery*, 42(1), 25–31.

Murphy, J., Boyle, F. (2010), Predicting neointimal hyperplasia in stented arteries using time-dependant computational fluid dynamics: a review, *Computers in biology and medicine*, 40(4), 408–418.

Nobili, M., Sheriff, J., Morbiducci, U., Redaelli, A., Bluestein, D. (2008), Platelet activation due to hemodynamic shear stresses: damage accumulation model and comparison to in vitro measurements, *ASAIO journal (American Society for Artificial Internal Organs: 1992)*, 54(1), 64.

Nordon, I., Hinchliffe, R., Holt, P., Loftus, I., Thompson, M. (2009), Modern treatment of juxtarenal abdominal aortic aneurysms with fenestrated endografting and open repair–a systematic review, *European Journal of Vascular and Endovascular Surgery*, 38(1), 35–41.

Odenstedt, H., Åneman, A., Oi, Y., Svensson, M., Stenqvist, O., Lundin, S. (2001), Descending aortic blood flow and cardiac output: A clinical and experimental study of continuous oesophageal echo-doppler flowmetry, *Acta anaesthesiologica scandinavica*, 45(2), 180–187.

Oderich, G. S., Greenberg, R. K., Farber, M., Lyden, S., Sanchez, L., Fairman, R., Jia, F., Bharadwaj, P., Investigators, Z. F. S. *et al*. (2014), Results of the united states multicenter prospective study evaluating the zenith fenestrated endovascular graft for treatment of juxtarenal abdominal aortic aneurysms, *Journal of vascular surgery*, 60(6), 1420–1428.

O'Donnell, T. F., Boitano, L. T., Deery, S. E., Schermerhorn, M. L., Schanzer, A., Beck, A. W., Green, R. M., Takayama, H., Patel, V. I. (2019), Open versus fenestrated endovascular repair of complex abdominal aortic aneurysms., *Annals of surgery*, .

O'neill, S., Greenberg, R., Haddad, F., Resch, T., Sereika, J., Katz, E. (2006), A prospective analysis of fenestrated endovascular grafting: intermediate-term outcomes, *European journal of vascular and endovascular surgery*, 32(2), 115–123.

Osinnski, J. N., Ku, D. N., Mukundan Jr, S., Loth, F., Pettigrew, R. I. (1995), Determination of wall shear stress in the aorta with the use of mr phase velocity mapping, *Journal of Magnetic Resonance Imaging*, 5(6), 640–647.

Ottesen, J. T., Olufsen, M. S., Larsen, J. K. (2004), *Applied mathematical models in human physiology*, SIAM.

Ou, J., Chan, Y. C., Cheng, S. W. (2015), A systematic review of fenestrated endovascular repair for juxtarenal and short-neck aortic aneurysm: evidence so far, *Annals of vascular surgery*, 29(8), 1680–1688.

Richter, G. M., Palmaz, J. C., Noeldge, G., Tio, F. (1999), Relationship between blood flow, thrombus, and neointima in stents, *Journal of vascular and interventional radiology*, 10(5), 598–604.

Sahni, O., Müller, J., Jansen, K. E., Shephard, M. S., Taylor, C. A. (2006), Efficient anisotropic adaptive discretization of the cardiovascular system, *Computer Methods in Applied Mechanics and Engineering*, 195(41-43), 5634–5655.

Suess, T., Anderson, J., Danielson, L., Pohlson, K., Remund, T., Blears, E., Gent, S., Kelly, P. (2016), Examination of near-wall hemodynamic parameters in the renal bridging stent of various stent graft configurations for repairing visceral branched aortic aneurysms, *Journal of vascular surgery*, 64(3), 788–796.

Šutalo, I. D., Lawrence-Brown, M. M., Ahmed, S., Liffman, K., Semmens, J. B. (2008), Modeling of antegrade and retrograde flow into a branch artery of the aorta: implications for endovascular stent-grafting and extra-anatomical visceral bypass, *Journal of Endovascular Therapy*, 15(3), 300–309.

Sutton, C. S., Oku, T., Harasaki, H., Kambic, H., Sugita, Y., Murabayashi, S., Shirey, E., Nose, Y. (1988), Titanium-nickel intravascular endoprosthesis: a 2-year study in dogs, *American Journal of Roentgenology*, 151(3), 597–601.

Textor, S. C., Lerman, L. O. (2015), Paradigm shifts in atherosclerotic renovascular disease: where are we now?, *Journal of the American Society of Nephrology*, 26(9), 2074–2080.

Tran, K., Fajardo, A., Ullery, B. W., Goltz, C., Lee, J. T. (2016), Renal function changes after fenestrated endovascular aneurysm repair, *Journal of vascular surgery*, 64(2), 273–280.

Ullery, B. W., Suh, G.-Y., Lee, J. T., Liu, B., Stineman, R., Dalman, R. L., Cheng, C. P. (2016), Comparative geometric analysis of renal artery anatomy before and after fenestrated or snorkel/chimney endovascular aneurysm repair, *Journal of vascular surgery*, 63(4), 922–929.

Verhoeven, E., Katsargyris, A., Bekkema, F., Oikonomou, K., Zeebregts, C., Ritter, W., Tielliu, I. (2015), Ten-year experience with endovascular repair of thoracoabdominal aortic aneurysms: results from 166 consecutive patients, *Journal of Vascular Surgery*, 61(5), 1378.

Verhoeven, E., Vourliotakis, G., Bos, W., Tielliu, I., Zeebregts, C., Prins, T., Bracale, U., van den Dungen, J. (2010), Fenestrated stent grafting for short-necked and juxtarenal abdominal aortic aneurysm: an 8-year single-centre experience, *European Journal of Vascular and Endovascular Surgery*, 39(5), 529–536.

Vignon-Clementel, I. E., Figueroa, C. A., Jansen, K. E., Taylor, C. A. (2006), Outflow boundary conditions for three-dimensional finite element modeling of blood flow and pressure in arteries, *Computer methods in applied mechanics and engineering*, 195(29-32), 3776–3796.

Vignon-Clementel, I. E., Figueroa, C., Jansen, K., Taylor, C. (2010), Outflow boundary conditions for 3d simulations of non-periodic blood flow and pressure fields in deformable arteries, *Computer methods in biomechanics and biomedical engineering*, 13(5), 625–640.

Weinstein, J. R., Anderson, S. (2010), The aging kidney: physiological changes, *Advances in chronic kidney disease*, 17(4), 302–307.

West, C. A., Noel, A. A., Bower, T. C., Cherry Jr, K. J., Gloviczki, P., Sullivan, T. M., Kalra, M., Hoskin, T. L., Harrington, J. R. (2006), Factors affecting outcomes of open surgical repair of pararenal aortic aneurysms: a 10-year experience, *Journal of vascular surgery*, 43(5), 921–928.

Williams, L., Leggett, R. (1989), Reference values for resting blood flow to organs of man, *Clinical Physics and Physiological Measurement*, 10(3), 187.

Xiao, N., Alastruey, J., Alberto Figueroa, C. (2014), A systematic comparison between 1-d and 3-d hemodynamics in compliant arterial models, *International journal for numerical methods in biomedical engineering*, 30(2), 204–231.

Youssefi, P., Gomez, A., Arthurs, C., Sharma, R., Jahangiri, M., Alberto Figueroa, C. (2018), Impact of patient-specific inflow velocity profile on hemodynamics of the thoracic aorta, *Journal of biomechanical engineering*, 140(1).